Geophysical Journal International

Geophys. J. Int. (2012) **190,** 1710–1722 doi: 10.1111/j.1365-246X.2012.05600.x

Source model of the 2009 M_w 7.6 Padang intraslab earthquake and its effect on the Sunda megathrust

Kelly Wiseman,[1] Paramesh Banerjee,[2] Roland Bürgmann,[1] Kerry Sieh,[2] Douglas S. Dreger[1] and Iwan Hermawan[2]

[1] *Department of Earth and Planetary Science, University of California, Berkeley, CA* 94720*, USA. E-mail: kelly@seismo.berkeley.edu*
[2] *Earth Observatory of Singapore, Nanyang Technological University, Singapore* 639798*, Singapore*

Accepted 2012 July 2. Received 2012 July 1; in original form 2011 December 21

SUMMARY

We investigate the source of the M_w 7.6 Padang earthquake by inverting three-component global positioning system (GPS) data and broad-band regional seismic-displacement waveforms. The earthquake involved oblique-reverse slip either on an E–W, south-dipping plane, or on a N–S, west-dipping plane. Finite-fault inversions indicate that the rupture primarily propagated downdip and southwest from the hypocentre, with a scalar seismic moment between 3.4 and 3.7 $\times$ 10^{20} N m (M_w 7.62–7.65). Analysis of the seismic and geodetic data do not allow for unique identification of the causative focal plane. Aftershock patterns strongly suggest the E–W plane was the causative focal plane, but aligned geological structures in the downgoing plate favour the N–S plane. In either case, this unusually large intraslab earthquake has moved closer to failure the deepest portion of the overlying megathrust, which last ruptured during a great earthquake more than two centuries ago and is late in its seismic cycle.

Key words: Earthquake source observations; Earthquake interaction, forecasting and prediction; Seismicity and tectonics; Subduction zone processes; Asia.

1 INTRODUCTION

The M_w 7.6 Padang earthquake of 2009 September 30 initiated ~250 km east of the Sunda trench at ~80 km depth. At this location the Hayes *et al.* (2009) Sunda slab model places the megathrust at ~69 km depth, thus, this event appears to have occurred within the downgoing oceanic plate. Large, intermediate depth, intraslab earthquakes, such as the 2001 M_w 6.8 Nisqually and 2001 M_w 7.7 El Salvador earthquakes, are often more devastating than comparable magnitude interplate earthquakes because they are located closer to the onshore population centres. They also tend to be normal fault events that can be explained by tension induced by bending of the slab or net slab pull (e.g. Vallée *et al.* 2003; Wada *et al.* 2010). The source of the Padang earthquake is particularly worthy of study for two reasons: the earthquake caused significant damage to the large coastal Sumatran city of Padang, and it was caused by unusual oblique-reverse rupture within the subducting oceanic plate beneath the decade's most seismically active megathrust (McCloskey *et al.* 2010). Moreover, the earthquake occurred just below a large span of that megathrust that appears from palaeoseismic evidence to be close to failure (Konca *et al.* 2008; Sieh *et al.* 2008).

The Sunda subduction zone arcs westward 6000 km from northwestern Australia, past Java, Sumatra and Myanmar to the eastern axis of the Himalayas. Along the 2000-km long segment off the west coast of Sumatra (Fig. 1), subduction is highly oblique, with 45–60 mm yr^{-1} of convergence (Simons *et al.* 2007) partitioned almost completely into strike-slip motion on the Sumatran fault and dip-slip motion on the megathrust (Fitch 1972; McCaffrey 1991).

Convergence along the Sunda arc involves two subducting plates: southeast of Sumatra the Australian plate dives northward beneath Java, whereas north of Sumatra the Indian plate subducts beneath the Andaman Sea. The boundary between the two subducting plates is a region of diffuse deformation so broad that it spans nearly the entirety of Sumatra, from at least 5.5°S to 2.5°N (e.g. Delescluse & Chamot-Rooke 2007). Most of the relative motion between the two oceanic plates appears to be occurring along north-striking, left-lateral strike-slip faults (Deplus *et al.* 1998; Deplus 2001), and some of these faults are being subducted. For example, one of these faults within the subducting slab may be associated with a persistent barrier to megathrust rupture at about 2.5°N (Meltzner *et al.* 2012). Another, the Investigator Fracture Zone (Fig. 1), appears to profoundly affect the character of subduction near the Equator (Fauzi *et al.* 1996; Natawidjaja *et al.* 2004). Finally, a subducting left-lateral fault was one of the sources of the M_w 7.9 Enggano earthquake that initiated the recent episode of Sumatran megathrust seismicity in 2000 (Abercrombie *et al.* 2003). Wharton Ridge, a fossil spreading centre, is another prominent bathymetric feature subducting near the Equator (Fig. 1). Magnetic anomaly data have shown that Wharton Ridge includes several east–west oriented fossil spreading segments (Liu *et al.* 1983; Deplus *et al.* 1998). Earthquakes within the Sumatran slab may initiate on reactivated faults associated with theses subducted Indian–Australian plate boundary structures.

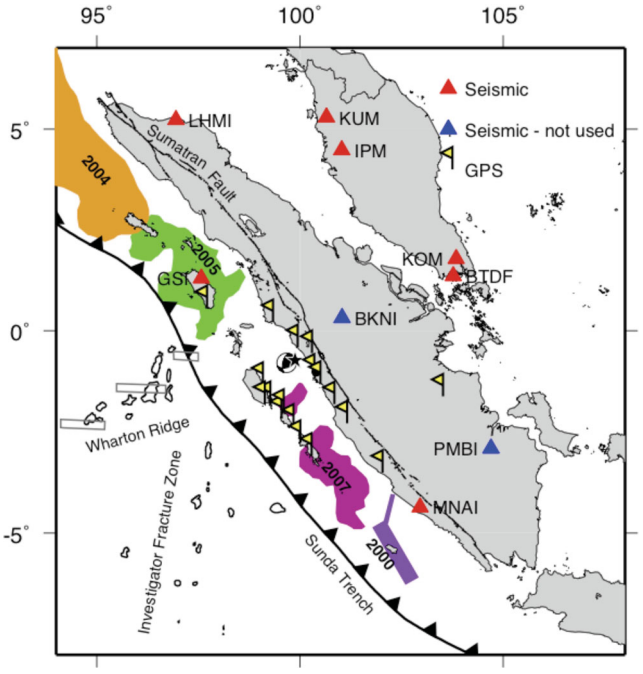

Figure 1. Context of the 2009 September 30 earthquake. Epicentre and focal mechanism are west of Padang. Great ruptures of 2000, 2004, 2005 and 2007 are in colour, projected to the surface from the underlying megathrust (Abercrombie *et al.* 2003; Chlieh *et al.* 2007; Konca *et al.* 2007; Konca *et al.* 2008). Red triangles signify stations with good seismic data that we use throughout the study, whereas blue triangles signify stations with corrupted seismic data. Yellow flags show the Sumatran GPS Array (SuGAr). The 4000 m bathymetry contours highlight the Investigator Fracture Zone and Wharton Ridge. The locations of east–west fossil spreading segments, deduced from magnetic anomalies (Deplus *et al.* 1998), are shown with grey rectangles.

One of the challenges associated with the 2009 Padang earthquake is determining the rupture geometry. Based on the global centroid moment tensor (GCMT) focal mechanism solution (www.globalcmt.org), the fault plane strikes either east–west with right-lateral oblique-reverse slip or north–south with left-lateral oblique slip. Possible candidates for the rupture plane could be subducted transform faults, fractures, or fossil spreading ridges (Liu *et al.* 1983; Deplus *et al.* 1998) associated with the diffuse Indian and Australian plate boundary. The USGS did not resolve which of these nodal planes was the rupture from their fitting of teleseismic broad-band *P* and *SH* waveforms and long-period surface waves (http://earthquake.usgs.gov/earthquakes/eqinthenews/2009/us2009mebz/finite_fault.php). We attempt to resolve the fault plane by using regional broad-band data, global positioning system (GPS) data and aftershock locations.

Nearly all the Sumatran section of the Sunda megathrust has ruptured in the past 7 yr. Thus far, the sequence has included the 2004 M_w 9.2 Aceh-Andaman earthquake (e.g. Chlieh *et al.* 2007; Shearer & Bürgmann 2010), the 2005 M_w 8.7 Nias-Simeulue earthquake (Konca *et al.* 2007), the 2007 M_w 8.4 Bengkulu earthquake (Konca *et al.* 2008) and a myriad of lesser events, including the damaging 2010 M_w 7.8 tsunami earthquake (Hill *et al.* 2012). One of the two large remaining unbroken sections of the Sumatran portion of the megathrust is a 350-km long section centred beneath Siberut Island, offshore of Padang (Chlieh *et al.* 2008) (Fig. 1). The Siberut segment has had a complex stress evolution during the past 7 yr, with megathrust ruptures to the northwest and southeast, two clusters of backthrust earthquakes in the upper plate above the section (Wiseman *et al.* 2011) and now a large, deep earthquake below the section. It is, therefore, especially important to understand the kinematics of the 2009 Padang earthquake to understand how it affects the stress levels on the Siberut segment of the megathrust and how it impacts seismic hazard in the region.

2 DATA

2.1 Broad-band waveforms

Nine three-component broad-band stations within 1000 km of the epicentre were operating at the time of the earthquake and have publicly available data (Fig. 1). The five Indonesian stations, BKNI, GSI, LHMI, MNAI and PMBI, are part of the GEOFON network and data from these stations were acquired through WebDC (http://webdc.eu). Data from BTDF of the Singapore National Network and IPM, KOM and KUM from the Malaysian National Seismic Network were obtained from IRIS (http://www.iris.edu).

The 27 acquired velocity waveforms appear in Fig. 2 with their instrument responses removed. Unfortunately, the largest amplitudes in the waveforms from the nearest seismic station, BKNI, are clipped. Therefore, we are not able to use the BKNI data in our seismic inversions. PMBI has suspect long-period motion, so we choose to exclude it from the inversions. Thus, there are seven stations with useable data that we integrate to displacement waveforms for our seismic inversions.

The data are first processed by removing the polezero instrument response and integrating to displacement. Both the displacement waveform data and the Green's functions were then bandpass filtered between 0.01 and 0.3 Hz. We use this bandpass because higher frequency components of the displacement waveforms are not resolvable using a 1-D velocity model. Lastly, we resample the data at 1.0 s. The maximum waveform amplitude for each component varies from about 0.4 to 1.4 cm.

2.2 Geodetic data

In our inversions, we include 3-component data from 18 permanent GPS stations ranging in distance from 37 to 417 km from the epicentre (Fig. 1, Table S1). The GPS stations are part of the Sumatran GPS Array (SuGAr; ftp://eos.ntu.edu.sg/SugarData/) and ENS-INSU regional networks (Hermawan 2010). Unfortunately, the data from the nearby ENS-INSU campaign GPS stations were noisy and with too large uncertainties to be useful in our inversions. Therefore we do not include campaign GPS data in the study. We used the GAMIT/GLOBK software package (Herring 2005; King & Bock 2005) to solve for daily station coordinates, and we calculated coseismic offsets using the tsview MATLAB toolbox (Herring 2003). Differencing of position time-series 10 d before and after the Padang earthquake yielded coseismic displacements at each site. We removed from the LNNG time-series a coseismic offset associated with a M_w 6.6 aftershock that occurred 15 hr after the Padang event on the Sumatran fault. That station, only 44 km from the epicentre of this earthquake, is the only station close enough to record a displacement from that event.

In general, the GPS sites along the western coast of the Sumatran mainland experienced coseismic subsidence and horizontal motion towards the earthquake's epicentre. The sites on the Mentawai islands, west of the epicentre, experienced uplift and horizontal motion away from the epicentre and towards the trench (Fig. 3). The

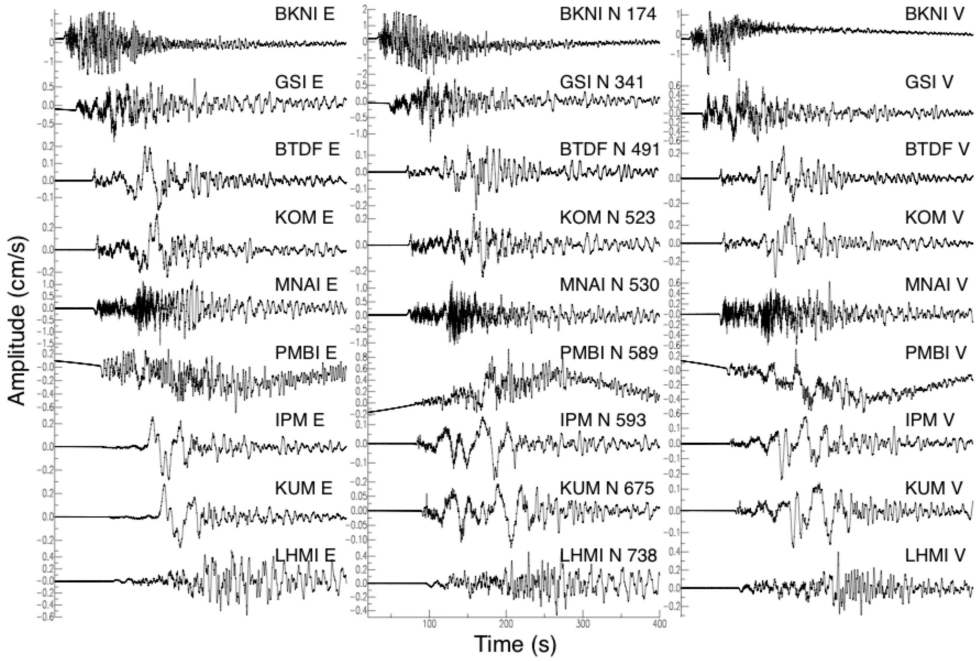

Figure 2. Observed velocity waveforms at all of the stations with publicly available data within 1000 km of the Padang epicentre. The epicentral distances (km) are labelled on the north components. The instrument responses have been removed from the data.

largest horizontal displacements, up to ∼5 cm, occurred at sites MSAI, TLLU and NGNG, on Siberut Island. The largest vertical displacement, ∼3 cm of subsidence, occurred on the west coast of Sumatra at site SCCN. However, the vertical measurements have large uncertainties that are comparable to the amplitude of the signal at most stations.

3 INVERSION METHOD

3.1 Model geometry

We use the geodetic data to constrain the input model geometry for the finite fault inversions. The geometry inversion method uses a constrained, non-linear optimization algorithm to solve for the best-fit, uniform-slip rectangular dislocation (Bürgmann *et al.* 1997) in an elastic half-space (Okada 1985). We used the GCMT nodal plane strike, dip and rake with fault dimensions based on Wells & Coppersmith (1994) scaling laws for our starting fault geometries. We loosely bounded the geometry inversion parameters: the strike and dip within 15° of the starting models, length within 50 km, width within 15 km and location within 1° latitude and longitude. Our optimal east-striking nodal plane (EWNP) fault geometry has a strike of 80° and dip of 57°, and the south-striking nodal plane (NSNP) has a strike of 190° and dip of 61°. Our geodetically constrained strike and dip values are within 6° of the GCMT moment tensor solution values for both nodal planes. The geodetic centroid for both nodal planes is located southeast of the GCMT centroid, ∼20 km south of the Engdahl relocated earthquake catalogue (EHB; E. R. Engdahl unpublished data using method of Engdahl *et al.* 2007) epicentre at an average of 78 km depth.

We adopt the optimal fault strike and dip parameters from the geometry inversion and solve for distributed slip with variable rake in the finite fault inversions. Our model fault plane extends 90 km along strike by 65 km downdip, divided into 5 km × 5 km patches. For the finite fault inversions, we assume the EHB epicentre with a depth of 78 km for our hypocentre location. Our hypocentre depth matches our geometry inversion centroid depth and the GCMT centroid depth. We did not use the EHB or National Earthquake Information Center (NEIC) catalogue depth for the hypocentre because both catalogues fix the hypocentre depth. We place the hypocentre within the central position along strike and 10 km downdip from the upper edge of the two modelled faults (cross-section view of fault planes shown in Fig. 5). This hypocentre location prevents slip from propagating shallower than the megathrust interface (shown in Fig. 11). The fault plane dimensions are extended from the geometry inversion to include the preferred geodetic centroid location south of the hypocentre.

3.2 Green's functions

The seismic Green's functions for our finite fault inversions are computed using a 1-D frequency-wavenumber integration method (Saikia 1994). We calculate Green's functions at 5-km distance intervals and at 4-km depth intervals. For our input earth model, we test two 1-D velocity models based on local earthquake travel-time tomography. The attenuation quality factors are from PREM (Dziewonski & Anderson 1981) and the density structure is similar to PREM but with higher crustal densities appropriate for the Sumatra region (Pollitz *et al.* 2006).

We first tested the minimum 1-D velocity model from Lange *et al.* (2010) (Table S4). The Lange *et al.* (2010) velocity model is inverted from local earthquake arrivals using a temporary deployment of land-stations and ocean bottom seismometers, as well as the GEOFON and BMKG permanent stations. The majority of the seismic stations span the ocean and Sumatran mainland between the latitudes of Nias and Siberut islands, just north of the Padang earthquake. The velocity model inversion is dominated by the large number of stations along the Sumatran Fault, with events located at crustal depths and in the Wadati Benioff zone, and is, therefore, a good model of Sumatran continental lithosphere velocity structure between 10 and 125 km depths.

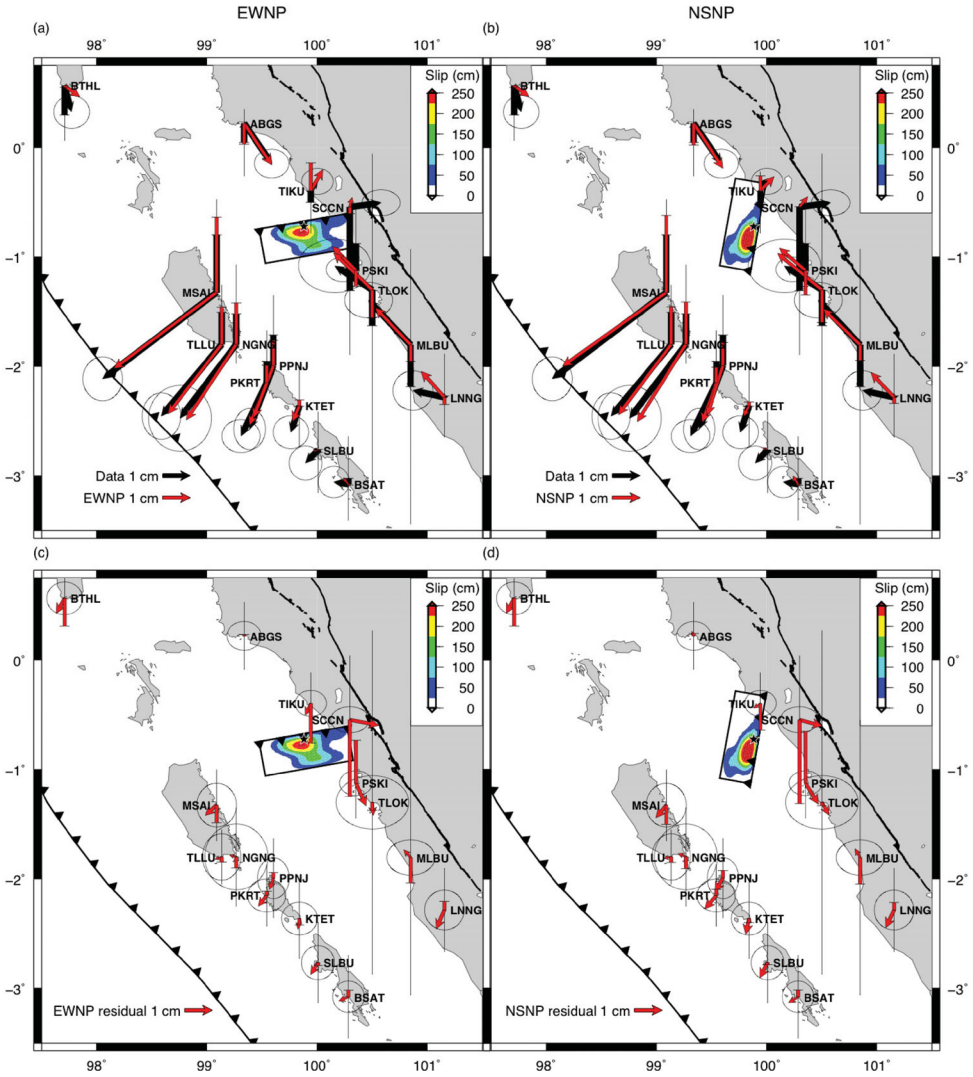

Figure 3. Comparison of GPS data and joint model displacement vectors for Panel (a) the east–west nodal plane (EWNP) and Panel (b) the north–south nodal plane (NSNP). Residuals between the joint model and GPS data are shown in (c) and (d). The corresponding distributed slip models are shown by colour contours on the fault planes projected to the surface.

Next we tested the minimum 1-D V_p model from Collings *et al.* (2012) with a range of V_p/V_s ratios from 1.8 to 1.9 (Table S5). The seismic stations for the Collings *et al.* study were deployed following the 2007 M_w 8.4 Bengkulu earthquake on the Mentawai islands and Sumatra mainland between 1°S and 4°S, just south of the Padang rupture. We find that a V_p/V_s ratio of 1.85 best fits our seismic data. The V_p velocities are higher in the Collings model than the Lange model, but the V_s velocities are lower. The Collings velocity structure has a few percent better variance reduction than the Lange velocity structure in our seismic inversions, and allows for less model smoothing (see Supplementary Materials). Therefore, we will use the Collings model throughout the rest of the study.

The Green's functions for the geodetic modelling are constructed using the programs EDGRN/EDCMP (Wang *et al.* 2003), on a layered half-space with the preferred Collings elastic structure.

3.3 Finite fault inversion method

We use a least-squares inversion method that employs simultaneous smoothing and damping to invert for finite fault slip (e.g. Hartzell & Heaton 1983; Kaverina *et al.* 2002). The technique inverts for fault slip over a grid of point sources that are triggered by a passing rupture front. We assume a circular rupture front and test a range of rupture velocities between 2.5 and 5.5 km s^{-1} (Fig. 4b). For the rupture velocity sensitivity tests, we use a dislocation rise time of 2.9 s, based on the scaling relationship between rise time and moment magnitude from Somerville *et al.* (1999). The modelled slip distribution shifts from high peak slip focused at the hypocentre to diffuse slip offset from the hypocentre when shifting from the lower to the higher range of the tested rupture velocities (Fig. S6). The variance reduction only differs by 2 per cent within the tested velocity range, peaking between 4.5 and 5.0 km s^{-1}. The small range of variance reductions does not warrant using super shear rupture velocities so we chose to use a lower rupture velocity of 4.0 km s^{-1}, equal to 0.9 times the shear wave velocity at the hypocentre, for the rest of the study.

Next, we tested the sensitivity of the seismic models to rise time. We tested values between 2.9 and 10.0 s (Fig. 4a). Shorter rise times are not resolvable using our 0.01–0.3 Hz bandpass. Variance reduction decreases with increasing rise time, and differs by 10 per cent between 2.9 and 10 s. Therefore, we use 2.9 s throughout the rest of

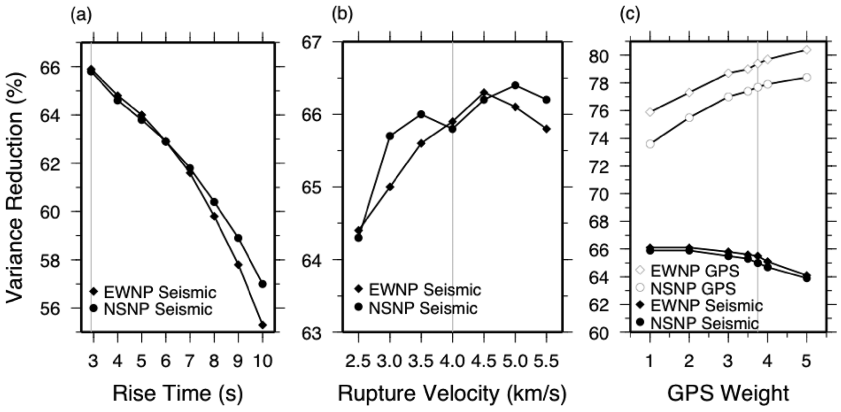

Figure 4. Seismic sensitivity tests. Panel (a) Variance reduction versus rise time. Panel (b) Variance reduction versus rupture velocity. Panel (c) Weight of the GPS data with respect to the seismic data (weight of 1) versus model fit. The preferred values are marked with grey lines.

the study, based on both the Sommerville *et al.* scaling relationship and our sensitivity test.

4 INVERSION RESULTS

4.1 Seismic waveform inversions

The initial finite fault inversion for both nodal plane geometries does a fairly good job of fitting the waveform amplitudes and polarities (Fig. S2a), with variance reductions for EWNP and NSNP both equal to 63 per cent. The peak slip region for EWNP is 15 km to the west and 10 km below the hypocentre (Fig. 5a). For NSNP, the peak slip region is 15 km to the south but starts just below the hypocentre (Fig. 5b). Both nodal planes have one peak slip region that tapers towards the model boundaries.

However, due to the use of a 1-D velocity model, there are artificial time-shifts between the Green's functions and the observed displacement waveforms. Therefore, we shifted the timing of the observations, between 1 and 6 s, so that the *S*-wave arrival aligns with the synthetic *S* wave at each site. By shifting the observation times, the variance reductions for both EWNP and NSNP improved to 66 per cent (Figs 5c and d). These time-shifts account for unmodelled heterogeneity in the actual velocity structure due to our use of a single 1-D velocity model for computing Green's functions.

There are no significant differences in waveform fit between the two nodal planes (Fig. S2b). They both fit all of the main waveform features except for the last high amplitude phase on the north component of stations BTDF and KOM. These stations are located close together, in Singapore and southern Malaysia, and the poor-fitting north component may be due to strong horizontal anisotropy along this azimuth, which is approximately perpendicular to the strike of the subducting slab.

The high-slip region for both nodal planes moves closer to the hypocentre after time-shifting the data. In addition, the slip distributions become more compact, with fewer fault patches requiring slip (Fig. 5). The total seismic moment for both nodal planes varies by only $\sim 3 \times 10^{18}$ N m, with EWNP moment equal to 3.79×10^{20} N m (M_w 7.65) and NSNP equal to 3.76×10^{20} N m (M_w 7.65). Although we allowed variable rake in the inversions, the rakes are very consistent at all of the fault patches with slip greater than 50 cm. For EWNP, the rake ranges from 133° to 155° for the patches with at least 50 cm of slip, and the slip-weighted average rake for all fault patches is 134°. For NSNP, the rake ranges from 30° to 51° for patches with at least 50 cm of slip and the slip-weighted average rake is 44°.

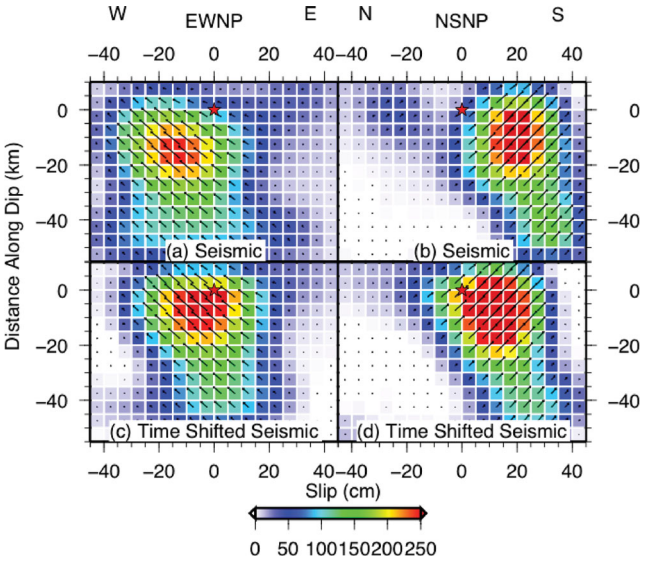

Figure 5. Comparison of slip distributions for seismic finite fault inversions: Panel (a, b) without time-shifts, and Panels (c, d) including variable station time-shifts (preferred). The peak slip regions for the time-shifted models are closer to the hypocentre than for the un-shifted models. The variance reductions also improve from 63 to 66 per cent for both EWNP and NSNP.

4.2 Geodetic inversions

In the GPS-only inversions, there are greater differences between the two modelled fault geometries than when using the seismic data (Fig. 6). The inverted slip distribution for EWNP is more sensitive to the smoothing coefficient than the slip distribution for NSNP. As you increase the weight put on the Laplacian smoothing constraint for EWNP, three high-slip asperities on the eastern corners and top western corner of the fault plane focus to a large, central slip distribution (Fig. S5). The preferred GPS EWNP model has a broader slip distribution, with lower peak slip than the GPS NSNP model or either seismic model (Figs 6a and b). Peak slip is ~20 km deeper in the GPS EWNP inversion than in the seismic inversion. Slip distribution along NSNP is very stable over a wide range of smoothing coefficients. Its slip is tightly focused, with a peak value of ~320 cm, ~130 cm higher than for EWNP. NSNP has a scalar

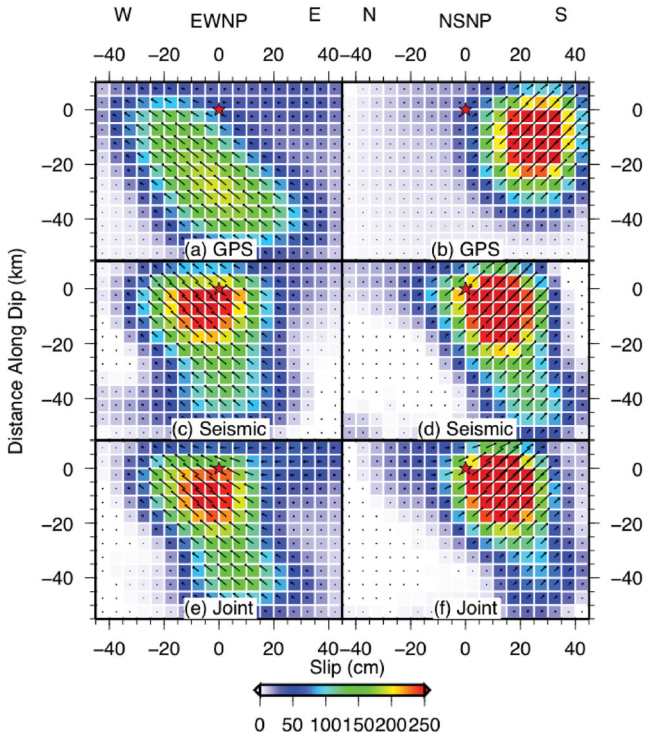

Figure 6. Slip distributions for the preferred finite-fault models, using the Collings velocity structure and variable station time-shifts. Panel (a) EWNP GPS-only inversion, Panel (b) NSNP GPS-only inversion, Panel (c) EWNP seismic-only inversion, Panel (d) NSNP seismic-only inversion, Panel (e) EWNP joint inversion, Panel (f) NSNP joint inversion. The red star is the EHB hypocentre. The arrows signify the variable rake orientations scaled by slip.

seismic moment of 3.19×10^{20} N m (M_w 7.60) and EWNP has a total moment of 3.76×10^{20} N m (M_w 7.65).

The total variance reduction for EWNP is 80 per cent and for NSNP is 78 per cent. The EWNP model fits all of the observed displacements within their 95 per cent confidence ellipse except for the three nearest stations on the west coast of Sumatra (TIKU, SCCN and PSKI) and BTHL on the southern tip of Nias (Fig. S3). The NSNP model fits all of the sites except SCCN, PSKI, BTHL and MSAI. A single fault plane with relatively smooth slip distribution, at the depth range of the subducting slab, cannot fit the complicated displacement field observed at the sites near Padang.

4.3 Joint inversions

Next, we combine the seismic waveform and GPS data to better constrain our inversions. There are data points every second for the seismic displacement data, with data time span ranging from 110 to 240 s for the seven 3-component stations. This totals 3960 seismic data points compared to 54 GPS data points for the 18 3-component stations. After normalizing for the difference in observation points, we optimized the data weights to get the smallest decrease in variance reduction when going from the individual to joint inversions. Fig. 4c shows how the seismic and geodetic model fits vary with increasing GPS data weight from 1.0 to 5.0 (with respect to seismic weight of 1.0). Using a GPS weight of 3.75 minimizes the decrease in variance reduction when going from the individual to joint inversions.

When using the GPS data weight of 3.75 and the same smoothing coefficient as with the independent seismic inversions, the seismic variance reduction stays at 66 per cent and the GPS variance reduction drops 1 per cent to 79 per cent for the joint EWNP inversion. The seismic variance reduction also drops 1 per cent to 65 per cent for the NSNP joint inversion and the GPS variance reduction continues to be 78 per cent. There are no notable differences between the waveforms synthetics for the individual and joint inversions (Fig. S2a and Fig. 7). The very similar independent and joint variance reductions show that the two data sets are consistent.

The EWNP joint slip distribution is more similar to the individual seismic model than to the GPS model (Figs 6a, c and e). The high-slip region stays the same and the lower-slip patches taper more towards the eastern edge of the fault in accordance with the GPS model. The scalar seismic moment for the joint inversion is 3.74×10^{20} N m (M_w 7.65), consistent with the individual moments. The same four GPS stations: BTHL, TIKU, SCCN and PSKI are not fit within uncertainties in the joint model (Figs 3a and c).

The NSNP joint slip distribution is a balance of the two independent slip distributions. The high-slip region starts just south of the hypocentre, like the seismic model, but there's less deep slip like the GPS model (Figs 6b, d and f). The scalar seismic moment for the joint inversion is 3.42×10^{20} N m (M_w 7.62), in between the two individual moments. The joint model fits the GPS station MSAI better and is now within the uncertainties. However, BTHL, SCCN and PSKI still do not fit within the uncertainties (Figs 3b and d).

For comparison, we calculate the best point source model searching over a range of source duration. The highest variance reduction is achieved using a duration of 15 s. The point source model is comparable to a finite source with a 60 km source dimension, which is similar to the dimension of the joint finite fault models. The point source model fits the GPS data nearly as well as the finite models, with total GPS data variance reduction of 68 per cent (Fig. S7). However, the seismic variance reduction is greatly reduced to 10 per cent (Fig. S8). The finite fault models improve the fit to the seismic data by accounting for the spatial variation in radiation pattern across the fault due to the variable slip and to a lesser extent variable rake.

5 AFTERSHOCKS

In Fig. 8, we have plotted one month of aftershocks following the Padang earthquake in both map view and depth section. Events are taken from the EHB catalogue, the NEIC catalogue and the International Data Center (IDC) catalogue [NEIC and IDC data retrieved from the International Seismological Centre (2011)]. There are no aftershocks large enough to have GCMT focal mechanisms within the first month. We have chosen to include multiple catalogues to balance the location accuracy with the number of events. The EHB catalogue has the highest location accuracy, but also the fewest number of events, with only 4 aftershocks greater than M_b 4.4. The NEIC catalogue includes 8 aftershocks greater than M_b 4.2. The IDC catalogue has the least certain locations, but includes events with magnitudes down to M_b 3.0, including 8 magnitude 4 events and 36 magnitude 3 events. We have plotted all of the events from the three catalogues on the map view figures, and only magnitude 4+ events on the depth section to exclude the large depth uncertainties associated with the magnitude 3 aftershocks. The map view figures highlight the preferential alignment of the aftershock epicentres with the strike of the EWNP. The depth sections emphasize the agreement between the larger magnitude aftershock locations and the EWNP high slip region (>150 cm slip) between 74 and 97 km depth.

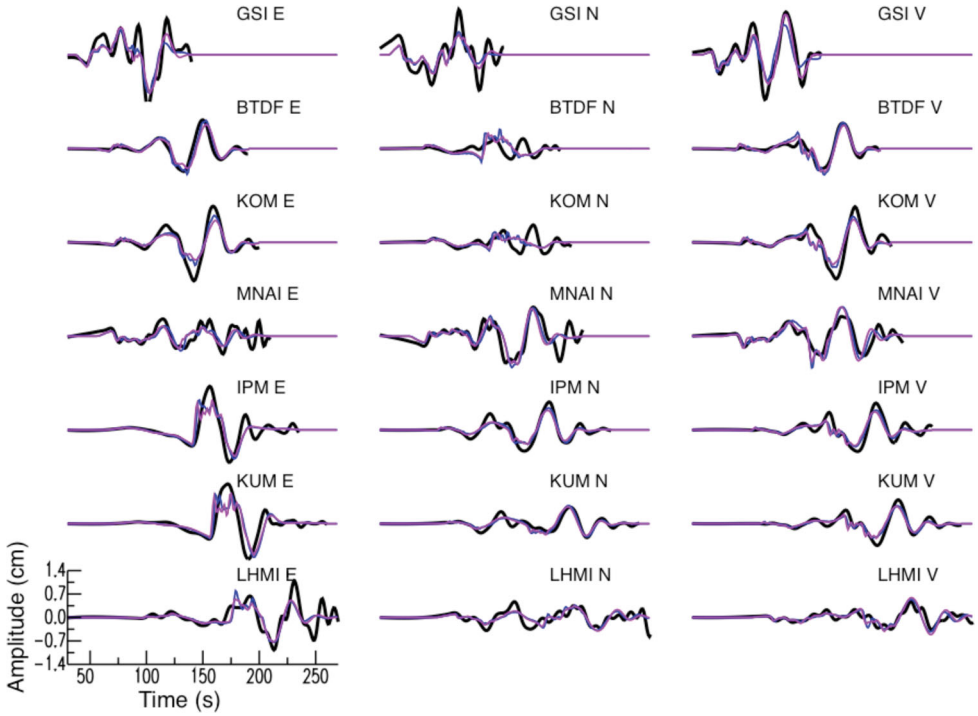

Figure 7. Displacement data and synthetics for the preferred joint finite fault models using Collings velocity structure with station time-shifts (cross-sections of slip distributions are shown in Figs 6e and f). The data is plotted in black, EWNP synthetics in blue and NSNP synthetics in magenta.

6 STRESS INTERACTIONS WITHIN THE SUBDUCTION ZONE

6.1 Induced stresses in the slab

Intraslab seismic activity has increased north of Padang, offshore of Sumatra, during the years following the 2004 Aceh-Andaman earthquake. We plot focal mechanisms from intraslab events before and after the 2004 megathrust earthquake in Fig. 9, selecting events from the GCMT catalogue (Global CMT Project 2011) that are at least 10 km below the Hayes *et al.* (2009) Sumatra slab interface. In addition, we identify and remove potentially mislocated interface events by removing mechanisms with an approximately trench parallel nodal plane, dip $< 35^\circ$ and rake between 60° and 120°. Prior to the 2004 earthquake, a majority of the intraslab activity occurred offshore of southern Sumatra, following the 2000 Enggano earthquake (Fig. 9a). The 2000 earthquake initiated in the slab and triggered a second subevent on the plate interface (Abercrombie *et al.* 2003). There was an especially energetic aftershock sequence following the 2000 earthquake, including both interface and intraslab events, which elevated seismicity levels above the background rate for a period lasting at least 4 yr (Wiseman & Bürgmann 2011).

Following the 2004 earthquake, intraslab activity increased beneath the 2004 and 2005 rupture zones (Fig. 9b). Intraslab activity also increased south of the 2005 Nias-Simeulue rupture, in the region east of Siberut. There were six intraslab events in this region below the unreleased Siberut section leading up to the 2009 Padang earthquake, between 2005 and 2008, in comparison to only 4 events between 1976 (the start of the catalogue) and 2004.

Static stress changes from the nearby 2005 and 2007 megathrust events enhanced the Coulomb Failure stress (CFS) in portions of the slab below the Siberut segment. We calculate the CFS changes in the slab from the recent megathrust earthquakes, and two nearby backthrust earthquake clusters (Wiseman *et al.* 2011), using our preferred Collings elastic structure and the EDGRN/EDCMP programs (Wang *et al.* 2003). ΔCFS is defined as the change in shear stress (positive in direction of fault slip) plus the effective coefficient of friction times the normal stress (unclamping is positive). Toda *et al.* (2011) found that 6 of the 7 largest, remote, off-megathrust Tohoku aftershocks experienced $\Delta\text{CFS} \geq 30$ kPa from the main shock. Stein (1999) concludes that 10 kPa is the minimum ΔCFS correlated with changes in seismicity rates. We assume an effective coefficient of friction $\mu' = 0.4$, and resolve the stress changes on a profile that extends from the trench to the western coast of Sumatra, through the 2009 hypocentre (A–A′ in Fig. 9b). Out of all the recent megathrust and backthrust earthquakes, the 2007 M_w 7.9 Bengkulu aftershock produced the largest positive CFS increase at the 2009 hypocentre, equal to 15 kPa. The 2007 earthquake produced a broad positive lobe encompassing the 2009 hypocentre, when resolved on the EWNP fault geometry, which also promoted two smaller intraslab events in 2007 and 2008 (Fig. 10). The other megathrust and backthrust events, even the 2009 backthrust cluster that started just 45 d before the Padang earthquake, produced <5 kPa at the 2009 hypocentre (Table 1, Fig. S9).

6.2 Induced stresses on the megathrust

We next model the stress changes on the megathrust due to the 2009 Padang earthquake to ascertain whether the section of the Sumatra megathrust between the 2005 and 2007 rupture zones, which last ruptured in the great Mentawai earthquake of 1797 (Natawidjaja *et al.* 2006), was relieved or enhanced. We calculate the shear, normal and CFS change at depth along the Hayes *et al.* (2009) slab interface. The slab interface steepens from 3° at 7.5 km depth to 45° at 115 km depth, and we assume a 90° rake and average strike for each depth interval ranging from 314° to 317°. Fig. 11 shows the CFS change on the megathrust due to slip on the EWNP, assuming an effective friction coefficient $\mu' = 0.4$ (stress changes

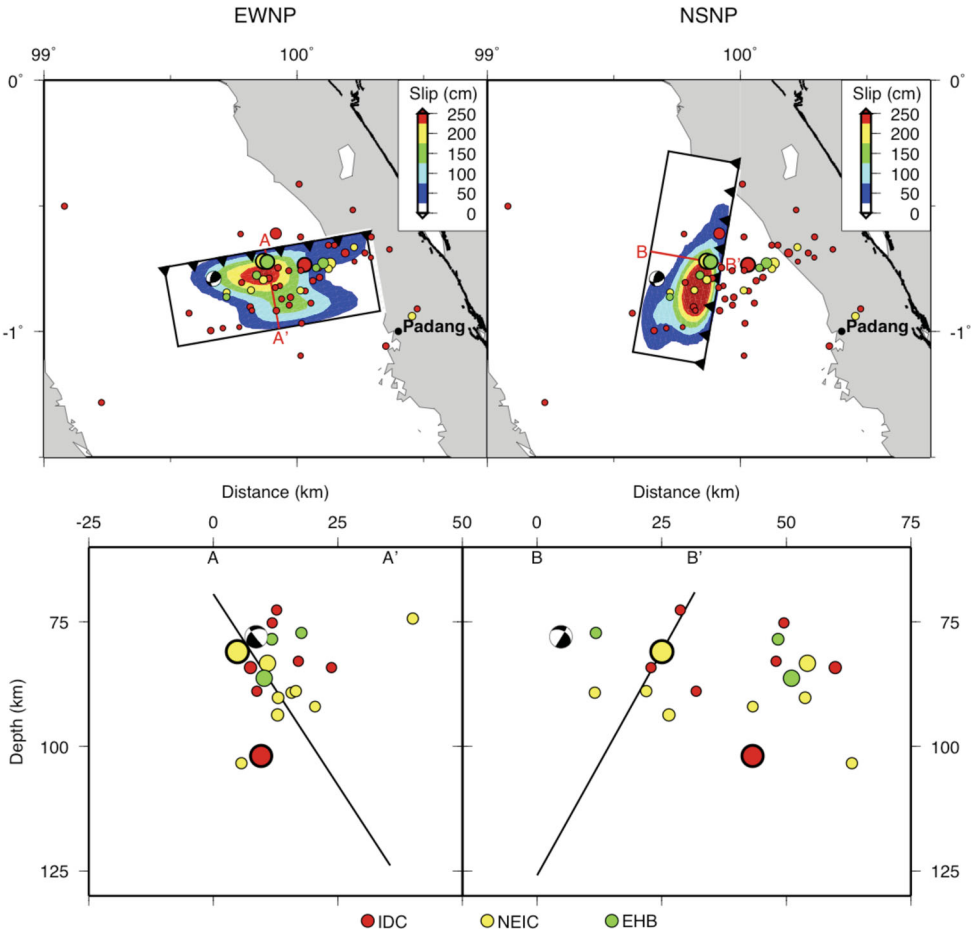

Figure 8. One month of aftershock activity following the 2009 main shock (boldly outlined in black). Aftershocks from three different seismic catalogues are shown: EHB (green), NEIC (blue) and IDC (red). The distributed slip models are shown by colour contours on the fault planes projected to the surface. The cross-sections restrict the EHB catalogue to only those events with accepted depths, and limit the IDC catalogue to $M_b \geq 4.0$ events.

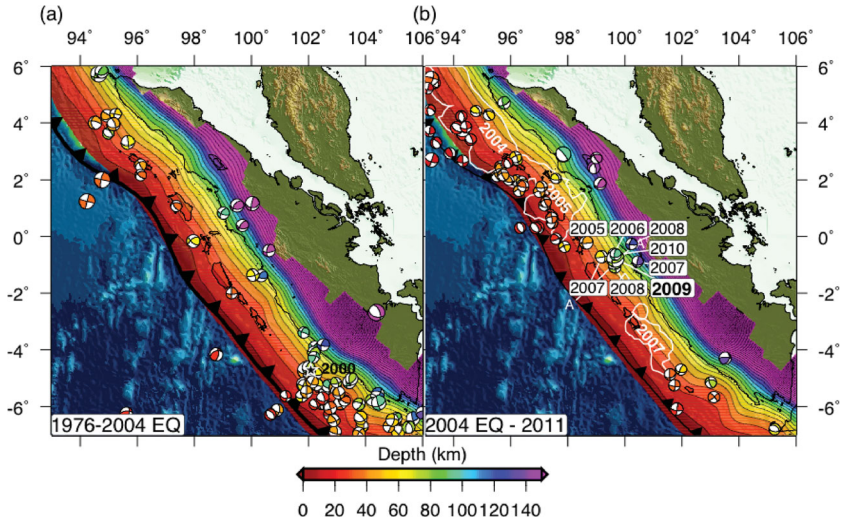

Figure 9. Intraslab focal mechanisms coloured according to hypocentral depth, beneath the Sunda megathrust, which is also colour-coded according to depth (from Hayes *et al.* 2009). Panel (a) 1976 until 2004 M_w 9.2 Aceh-Andaman earthquake. The location of the 2000 M 7.9 Enggano earthquake is shown with black star. Panel (b) After the 2004 earthquake until 2011 May. The rupture zones for the three great earthquakes of 2004, 2005 and 2007 are outlined in white. The years are listed for the events near the 2009 earthquake. All plotted centroids are at least 10 km below the megathrust interface.

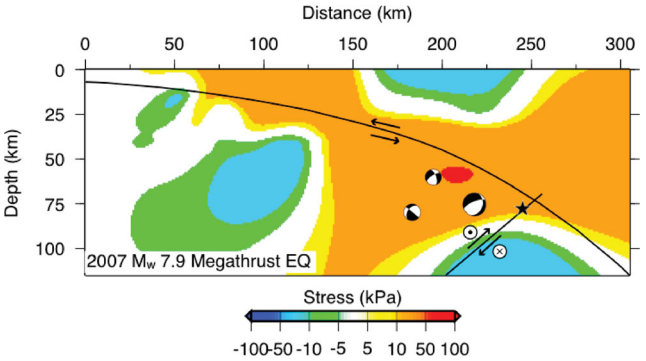

Figure 10. Stress changes resolved on the EWNP fault geometry, resulting from the 2007 M_w 7.9 Bengkulu aftershock (Konca *et al.* 2008). The cross-section is perpendicular to the trench and extends through the 2009 hypocentre (profile A–A′ shown on Fig. 9b). Intraslab earthquake focal mechanisms following the 2007 Bengkulu earthquake up to and including the 2009 Padang earthquake, overlay the cross-section. Note the non-linear stress scale.

due to slip on the NSNP are shown in Fig. S10). We model a similar stress pattern as the McCloskey *et al.* (2010) study, with strong stress relaxation over the rupture plane, with surrounding lobes of moderate loading. The stress shadow is large on the megathrust directly over the hypocentre, and peaks at over −1 MPa, a significant proportion of typical earthquake stress drops. The stress shadow continues ∼85 km southwest towards Siberut at over −10 kPa. CFS is enhanced by over 1 MPa directly north of the fault plane. The interface continues to be loaded to the northwest by at least 10 kPa to 40 km depth and south of the rupture plane by at least 10 kPa to 45 km depth. The stress cross-sections show unclamping of the megathrust further updip from the 2009 hypocentre in the seismogenic zone near Siberut, but shear stress and CFS are reduced in this region, as we prevent the intraslab fault from slipping through the megathrust interface.

7 DISCUSSION

Our joint analysis of geodetic and seismic waveform data confirms that the Padang earthquake was not caused by rupture of the Sunda megathrust. It initiated in the subducting slab at ∼80 km depth, near the plate interface, and ruptured primarily downdip and to the southwest. Our joint modelling does not favour either the N–S or the E–W nodal plane as the source of the earthquake—variance reductions for the two nodal planes are equivalent. Moreover, the synthetic waveforms for each nodal plane are very similar in amplitude, frequency content and polarities. The NSNP has very slightly lower GPS displacement residuals in the joint inversion (one fewer near-field site falls outside the errors), but this is not a compelling reason to favour the N–S nodal plane. This is a similar situation to the 2001 Nisqually intraslab earthquake models, where inversion of both seismic and geodetic data could not resolve the fault plane ambiguity (Ichinose *et al.* 2004).

Reinforcing the ambiguity are two other pieces of information. The east–west alignment of aftershocks, and their depth range,

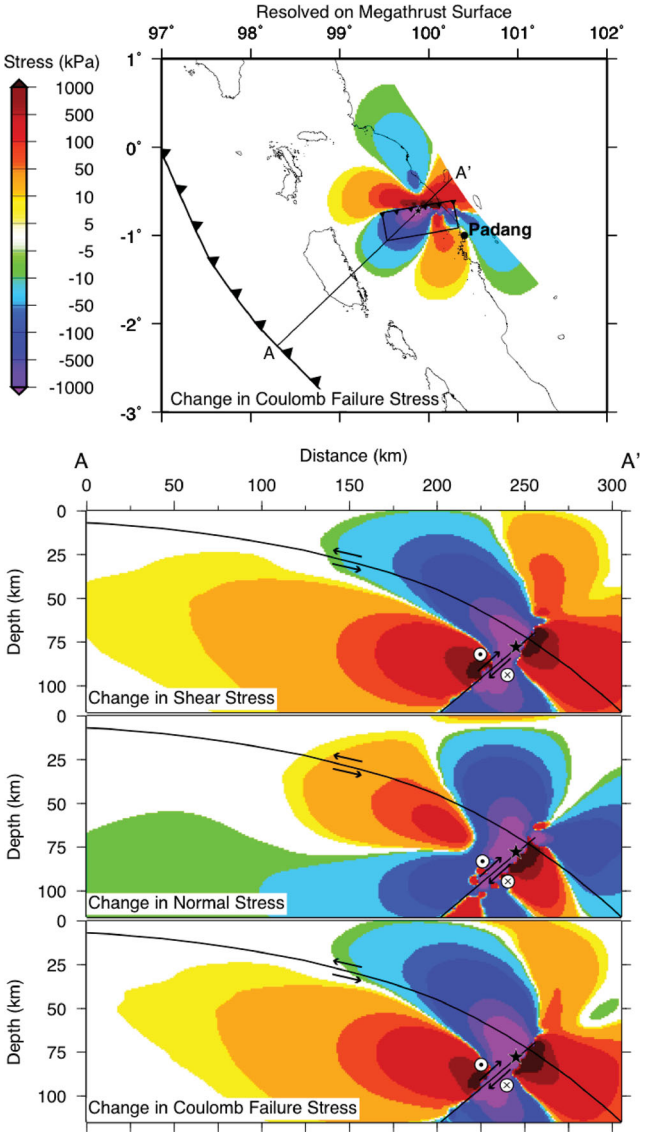

Figure 11. Stress changes resulting from slip on the EWNP resolved on the megathrust. The map shows CFS change on the megathrust assuming $\mu' = 0.4$. The cross-sections are perpendicular to the trench and extend through the 2009 hypocentre and show shear stress change, normal stress change and CFS change (the corresponding stress models for the NSNP are shown in Fig. S10). Note the non-linear stress scale.

favours the east–west rupture, but geological context favours the north–south rupture. The N10°E orientation of NSNP aligns well with the N03°E fabric of fracture zones on the subducting seafloor. NSNP is just east of the most pronounced of these fractures—the Investigator Fracture Zone (Fig. 1). Fauzi *et al.* (1996) showed that the subducted portion of the Investigator Fracture Zone near Toba had high levels of seismicity. Several of the other N–S striking structures are active on the seafloor west of the Sunda trench (Deplus *et al.* 1998). Moreover, at least one is active within the

Table 1. CFS changes (kPa) at the 2009 Padang earthquake hypocentre due to recent large earthquakes.

Fault geometry	2004 Aceh-Andaman	2005 Nias-Simeulue	2005 backthrust	2007 M_w 8.4 Bengkulu	2007 M_w 7.9 Bengkulu	2009 backthrust
EWNP	<−1	−1	3	<1	15	2
NSNP	−1	−3	1	−5	22	1

subducting slab: Left-lateral rupture of a subducted N–S fracture zone initiated the M_w 7.9 Enggano Island earthquake of June 2000 (Abercrombie *et al.* 2003). Thus it is quite plausible that the 2009 Padang earthquake was the result of rupture on a north-striking, left-lateral oceanic fracture zone. This hypothesis is supported by the dip of the NSNP. If an oceanic fracture zone has been subducted within the oceanic lithosphere, its dip should be rotated from verticality by an amount associated with the dip of the overlying megathrust. Using the stereonet program OSXStereonet (http://homepage.mac.com/nfcd/work/programs.html), we have determined the orientation of the north-striking fractures once they've been subducted to the location of the 2009 earthquake. Above the hypocentre of the 2009 earthquake, the dip of the megathrust is about 32° to the northeast (Hayes *et al.* 2009), and considering the 47° angle between the strike of the megathrust and the N03°E strike of the fracture zones on the ocean floor, the rupture plane beneath the megathrust should strike N08°E and dip 69° west. This is very close to the N10°E strike and 61°W dip of our optimal NSNP.

An alternative hypothesis favouring the EWNP is that the earthquake was caused by rupture of a subducted normal fault associated with the Wharton Ridge fossil spreading centres (grey rectangles on Fig. 1, from Deplus *et al.* 1998). The fossil spreading centres west of the Sunda trench, are orientated 14° southeast of the EWNP. Assuming that the normal faults initially dip 60°, the subducted fault would strike N71°E with a 40° dip. Our optimal EWNP strikes N80°E and dips 57°, thus the reoriented normal faults are not as close of a match to the EWNP as the vertical fractures are to the NSNP.

We mentioned above that the 2009 Padang earthquake is similar to the M_w 7.9 2000 Enggano earthquake, offshore of southern Sumatra. One intriguing aspect of the 2000 earthquake is that it involved two subevents. Abercrombie *et al.* (2003) concluded from analysis of teleseismic body waves and aftershock mechanisms that the earthquake initiated as a north–south oriented, left-lateral rupture of the downgoing Australian plate but concluded with rupture of an overlying patch of the megathrust. The Padang aftershock sequence is much less energetic than the 2000 sequence and there is no differentiated class of shallower, megathrust aftershocks in the NEIC, IDC or GCMT catalogues to suggest there may have been a subevent on the megathrust. In addition, there are no detectable post-seismic transients in the geodetic data following the 2009 earthquake, and therefore no observable triggered aseismic slip on the megathrust. This lack of post-seismic afterslip on the megathrust suggests that the interface is still strongly coupled deeper than 55 km, where there was >0.1 MPa stress increase north of the rupture plane.

The Siberut section of the Sunda megathrust has had a complex stress evolution over the past 7 yr. The 2004 and 2005 megathrust earthquakes enhanced CFS above 10 kPa until the southern end of the Batu Islands (Fig. 12a). The two backthrust clusters in 2005 and 2009 decreased CFS on the shallow portion of the megathrust, surrounding Siberut, but increased CFS on the deeper section (Fig. 12b). The 2007 Bengkulu earthquakes greatly enhanced CFS on the section of the megathrust that didn't rupture between the M_w 8.4 and M_w 7.9 earthquakes, and also remained above 10 kPa between central Siberut and western Sumatra (Fig. 12c). When adding the contribution of the 2009 Padang earthquake to the stress field, the Siberut segment has experienced >10 kPa coseismic CFS change over a majority of the segment over the past 7 yr (Fig. 12d). Chlieh *et al.* (2008) inverts geodetic data to determine interseismic coupling along the megathrust and determines that the megathrust is poorly coupled beneath the Batu Islands, which can explain the southern boundary of the 2005 Nias-Simeulue earthquake. However, the megathrust appears to be strongly coupled beneath Siberut, Sipora and Pagai Islands until at least 50 km depth. In

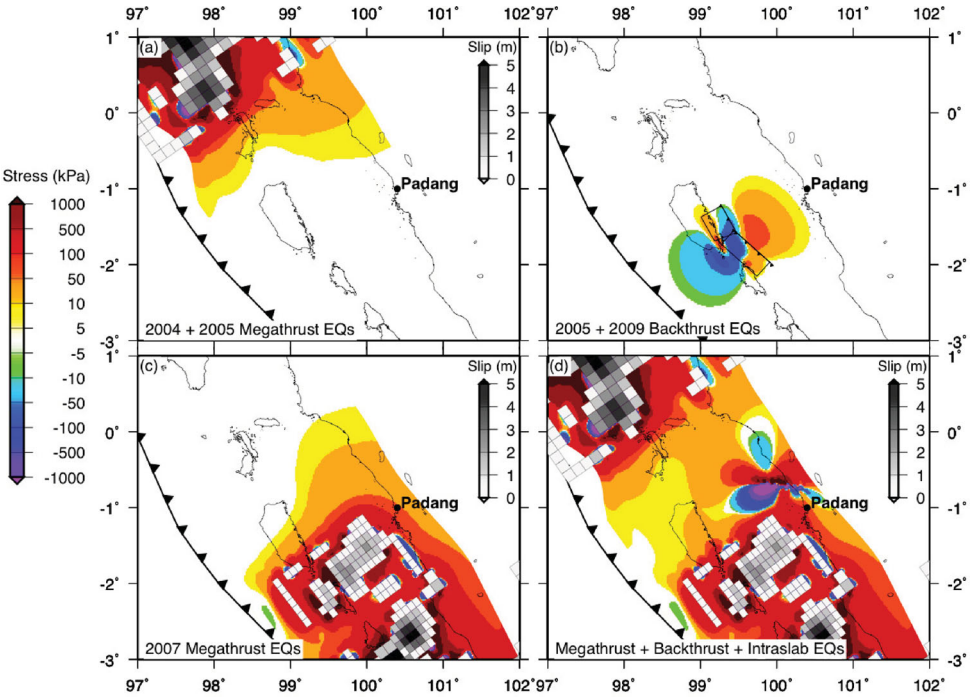

Figure 12. Stress changes resolved on the megathrust, resulting from Panel (a) the combined 2004 M_w 9.2 (Chlieh *et al.* 2007) and 2005 M_w 8.7 (Konca *et al.* 2007) megathrust earthquakes, Panel (b) the combined 2005 and 2009 M_w 6.7 backthrust earthquakes (Wiseman *et al.* 2011), Panel (c) the combined 2007 M_w 8.4 and M_w 7.9 earthquakes (Konca *et al.* 2008) and Panel (d) all of the events in Panels (a–c) and the 2009 M_w 7.6 intraslab earthquake. The map shows CFS change on the megathrust assuming $\mu' = 0.4$. The slip models for the megathrust events overly the stress changes, signifying the portions of the megathrust with large coseismic stress drop. Note the non-linear stress scale.

addition, more slip deficit has accumulated near Siberut since 1797 than the maximum coseismic slip estimates for the 1797 event (Konca *et al.* 2008; Chlieh *et al.* 2008). Therefore, the Siberut segment, which palaeoseismic data suggest is overdue for another great earthquake, and has been pushed closer to failure from all directions during the past 7 yr, appears to have the highest seismic hazard in the region.

8 CONCLUSIONS

Our seismic waveform and geodetic analysis shows that the Padang earthquake initiated in the subducting slab and extended downdip of the hypocentre to the southwest, although our analysis can not determine which nodal plane was the rupture surface. The aftershock catalogues align better with the strike of the east–west plane, which may be the most conclusive evidence available. Both nodal planes align with prominent bathymetric features: the north–south plane with the strike-slip faults near the Investigator Fracture Zone, and to a lesser degree, the east–west plane with Wharton Ridge and associated normal faults. The Padang earthquake is the second largest intraslab earthquake in the Sunda subduction zone recorded in the GCMT catalogue, behind the 2000 Enggano earthquake. Intraslab activity increased below the Siberut segment of the megathrust during the years following the 2004 Aceh-Andaman earthquake, with eight events producing oblique focal mechanisms between 2005 and 2010. The 2009 Padang earthquake has variably stressed the deepest portion of the coupled megathrust, encouraging rupture northwest and south of the 2009 fault plane and discouraging rupture directly over and to the southwest of the fault plane. This Siberut section of the megathrust last participated in a major rupture either in 1797 or about a century earlier and appears from palaeoseismic evidence to be poised for another great rupture. The 2009 earthquake may encourage the next Sumatran megathrust event to initiate in the northern portion of the historic 1797 rupture, south of the 2005 Nias rupture and just north of Siberut.

ACKNOWLEDGMENTS

This work has been supported in part by NSF grant EAR-0738299 (to Roland Bürgmann). The SuGAr permanent GPS data have been supported by Nanyang Technological University's Earth Observatory of Singapore. Thanks to Christophe Vigny for contributing to early discussions on the Padang earthquake. Most of the figures in this paper were produced using the generic mapping tools (GMT). This is Berkeley Seismological Laboratory contribution 11.09 and Earth Observatory of Singapore contribution 39.

REFERENCES

Abercrombie, R.E., Antolik, M.A. & Ekstrom, G., 2003. The June 2000 M_w 7.9 earthquakes south of Sumatra: deformation in the India-Australia Plate, *J. geophys. Res.,* **108,** doi:10.1029/2001JB0000674.

Bürgmann, R., Segall, P., Lisowski, M. & Svarc, J., 1997. Postseismic strain following the 1989 Loma Prieta earthquake from GPS and leveling measurements, *J. geophys. Res.,* **102,** 4933–4955.

Chlieh, M. *et al*., 2007. Coseismic slip and afterslip of the great M_w 9.15 Sumatra-Andaman earthquake of 2004, *Bull. seism. Soc. Am.,* **97,** S152–S173.

Chlieh, M., Avouac, J.P., Sieh, K., Natawidjaja, D.H. & Galetzka, J., 2008. Heterogeneous coupling of the Sumatran megathrust constrained by geodetic and paleogeodetic measurements, *J. Geophys. Res.,* **113,** B05305, doi:10.1029/2007JB004981.

Collings, R., Lange, D., Rietbrock, A., Tilmann, F., Natawidjaja, D., Suwargadi, B., Miller, M. & Saul, J., 2012. Structure and seismogenic properties of the Mentawai segment of the Sumatra subduction zone revealed by local earthquake travel-time tomography, *J. geophys. Res.,* **117,** B01 312, doi:10.1029/2011JB008469.

Delescluse, M. & Chamot-Rooke, N., 2007. Instantaneous deformation and kinematics of the India-Australia Plate, *Geophys. J. Int.,* **168,** 818–842.

Deplus, C. *et al*., 1998. Direct evidence of active deformation in the eastern Indian oceanic plate, *Geology,* **26,** 131–134.

Deplus, C., 2001. Indian ocean actively deforms, *Science,* **292,** 1850–1851.

Dziewonski, A.M. & Anderson, D.L., 1981. Preliminary reference earth model, *Phys. Earth planet. Inter.,* **25,** 297–356.

Engdahl, E.R., Villasenor, A., DeShon, H.R. & Thurber, C.H., 2007. Teleseismic relocation and assessment of seismicity (1918–2005) in the region of the 2004 M_w 9.0 Sumatra-Andaman and 2005 M_w 8.6 Nias Island great earthquakes, *Bull. seism. Soc. Am.,* **97,** S43–S61, doi:10.1785/0120050614.

Fauzi, McCaffrey, R., Wark, D., Sunaryo, P.Y. & Prih Haryadi, P.Y., 1996. Lateral variation in slab orientation beneath Toba Caldera, northern Sumatra, *Geophys. Res. Lett.,* **23**(5), 443–446.

Fitch, T.J., 1972. Plate convergence, transcurrent faults, and internal deformation adjacent to Southeast Asia and Western Pacific, *J. geophys. Res.,* **77**(23), 4432–4460.

Global CMT Project, 2011. Global CMT catalog. Available at: www.globalcmt.org (last accessed 2011 April 30).

Hartzell, S.H. & Heaton, T.H., 1983. Inversion of strong ground motion and teleseismic waveform data for the fault rupture history of the 1979 Imperial Valley, California, earthquake, *Bull. seism. Soc. Am.,* **73,** 1553–1583.

Hayes, G.P., Wald, D.J. & Keranen, K., 2009. Advancing techniques to constrain the geometry of the seismic rupture plane on subduction interfaces a priori: higher-order functional fits, *Geochem. Geophys. Geosyst.,* **10,** doi:10.1029/2009GC002633.

Hermawan, I., 2010. Sismotectonique des failles actives en Indonésie, vue par géodésie spatiale, *PhD thesis,* Ecole Normale Superieure, Paris.

Herring, T., 2003. MATLAB Tools for viewing GPS velocities and time series, *GPS Solutions,* **7,** 194–199, doi:10.1007/s10291-003-0068-0.

Herring, T.A., 2005. GLOBK, Global Kalman filter VLBI and GPS analysis program, release 10.2, Massachusetts Institute of Technology, Cambridge, MA.

Hill, E.M. *et al*., 2012. The 2010 M_w 7.8 Mentawai earthquake: very shallow source of a rare tsunami earthquake determined from tsunami field survey and near-field GPS data, *J. geophys. Res.,* **117,** doi:10.1029/2012JB009159.

Ichinose, G.A., Thio, H.K. & Somerville, P.G., 2004. Rupture process and near-source shaking of the 1965 Seattle-Tacoma and 2001 Nisqually, intraslab earthquakes, *Geophs. Res. Lett.,* **31,** doi:10.1029/004GL019668.

International Seismological Centre, 2011. *On-line Bulletin*, Available at: http://www.isc.ac.uk (last accessed 2011 October 15).

Kaverina, A., Dreger, D. & Price, E., 2002. The combined inversion of seismic and geodetic data for the source process of the 16 October 1999 M_w 7.1 Hector Mine, California, earthquake, *Bull. seism. Soc. Am.,* **92,** 1266–1280.

King, R. & Bock, Y., 2005. Documentation for the GAMIT GPS analysis software, release 10.2, Massachusetts Institute of Technology, Cambridge, MA.

Konca, A.O. *et al*., 2007. Rupture kinematics of the 2005 M_w 8.6 Nias-Simeulue earthquake from the joint inversion of seismic and geodetic data, *Bull. seism. Soc. Am.,* **97,** S307–S322.

Konca, A.O. *et al*., 2008. Partial rupture of a locked patch of the Sumatra megathrust during the 2007 earthquake sequence, *Nat. Geosci.,* **456,** 631–635.

Lange, D. *et al*., 2010. The fine structure of the subducted investigator fracture zone in Western Sumatra as seen by local seismicity, *Earth planet. Sci. Lett.,* **298,** 47–56.

Liu, C., Curray, J.R. & McDonald, J.M., 1983. New constraints on the tectonic evolution of the eastern Indian Ocean, *Earth planet. Sci. Lett.,* **65,** 331–342.

McCaffrey, R., 1991. Slip vectors and stretching of the Sumatran Fore Arc, *Geology,* **19**(9), 881–884.

McCloskey, J., Lange, D., Tilmann, F., Nalbant, S.S., Bell, A.F., Natawidjaja, D.H. & Rietbrock, A., 2010. The September 2009 Padang earthquake, *Nat. Geosci.,* **3,** 70–71.

Meltzner, A.J., Sieh, K., Chiang, H.-W., Shen, C.-C., Suwargadi, B.W., Natawidjaja, D.H., Philibosian, B. & Briggs, R.W., 2012. Persistent Termini of 2004- and 2005-like Ruptures of the Sunda Megathrust, *J. geophys. Res.,* **117,** doi:10.1029/2011JB008888.

Natawidjaja, D., Sieh, K., Ward, S., Cheng, H., Edwards, R., Galetzka, J. & Suwargadi, B., 2004. Paleogeodetic records of seismic and aseismic subduction from central Sumatran microatolls, Indonesia, *J. geophys. Res.,* **109,** doi:10.1029/2003JB002398.

Natawidjaja, D.H. *et al*., 2006. Source parameters of the great Sumatran megathrust earthquakes of 1797 and 1833 inferred from coral microatolls, *J. geophys. Res.,* **111,** B06403, doi:10.1029/2005JB004025.

Okada, Y., 1985. Surface deformation due to shear and tensile faults in a half-space, *Bull. seism. Soc. Am.,* **75,** 1135–1154.

Pollitz, F.F., Bürgmann, R. & Banerjee, P., 2006. Post-seismic relaxation following the great 2004 Sumatra-Andaman earthquake on a compressible self-gravitating Earth, *Geophys. J. Int.,* **167,** 397–420, doi:10.1111/j.1365-246X.2006.03018.x.

Saikia, C.K., 1994. Modified frequency-wave number algorithm for regional seismograms using Filon's quadrature-modeling of L(g) waves in eastern North America, *Geophys. J. Int.,* **118,** 142–158.

Shearer, P.M. & Bürgmann, R., 2010. Lessons learned from the 2004 Sumatra-Andaman megathrust rupture, *Ann. Rev. Earth planet. Sci.,* **38,** 103–131.

Sieh, K. *et al*., 2008. Earthquake supercycles inferred from sea-level changes recorded in the corals of West Sumatra, *Science,* **322,** 1674–1678.

Simons, W.J.F. *et al*., 2007. A decade of GPS in Southeast Asia: resolving Sundaland motion and boundaries, *J. geophys. Res.,* **112,** B06420, doi:10.1029/2005JB003868.

Somerville, P.G. *et al*., 1999. Characterizing crustal earthquake slip models for the prediction of strong ground motion, *Seism. Res. Lett.,* **70,** 59–80.

Stein, R.S., 1999. The role of stress transfer in earthquake occurrence, *Nature,* **402,** 605–609.

Toda, S., Lin, J. & Stein, R.S., 2011. Using the 2011 M = 9.0 Tohoku earthquake to test the Coulomb stress triggering hypothesis and to calculate faults brought closer to failure, *Earth Planets Space,* **63,** doi:10.5047/eps.2011.05.010.

Vallée, M., Bouchon, M. & Schwartz, S.Y., 2003. The 13 January El Salvador earthquake: a multidata analysis, *J. geophys. Res.,* **108,** doi:10.1029/2002JB001922.

Wada, I., Mazzotti, S. & Wang, K., 2010. Intraslab stresses in the Cascadia subduction zone from inversion of earthquake focal mechanisms, *Bull. seism. Soc. Am.,* **100,** 2002–2013.

Wang, R., Martin, F.L. & Roth, F., 2003. Computation of deformation induced by earthquakes in a multi-layered elastic crust – FORTRAN programs EDGRN/EDCMP, *Comput. Geosci.,* **29,** 195–207.

Wells, D.L. & Coppersmith, K.J., 1994. New empirical relationships among magnitude, rupture length, rupture width, rupture area, and surface displacement, *Bull. seism. Soc. Am.,* **84,** 974–1002.

Wiseman, K. & Bürgmann, R., 2011. Stress and seismicity changes on the Sunda megathrust preceding the 2007 M_w 8.4 Earthquake, *Bull. seism. Soc. Am.,* **101,** 313–326.

Wiseman, K., Banerjee, P., Sieh, K., Bürgmann, R. & Natawidjaja, D.H., 2011. Another potential source of destructive earthquakes and tsunami offshore of Sumatra, *Geophys. Res. Lett.,* **38,** doi:10.1029/2011GL047226.

SUPPORTING INFORMATION

Additional Supporting Information may be found in the online version of this article:

Figure S1. Displacement data and synthetics for the seismic finite fault model using Lange earth model (Table S4). The data is plotted in black, E–W nodal plane (EWNP) synthetics in blue and N–S nodal plane (NSNP) synthetics in magenta. The models use a smoothing coefficient of 2.5×10^{-6} and have total seismic variance reductions of 58 per cent for EWNP and 55 per cent for NSNP.

Figure S2. Comparison of displacement data and synthetics for the seismic finite fault models using: Panel (a) Collings earth model (Table S5) with total seismic variance reductions of 63 per cent for EWNP and 63 per cent for NSNP and Panel (b) Collings earth model with variable time-shifts (preferred) with total seismic variance reduction improving to 66 per cent for EWNP and 66 per cent for NSNP. The data is plotted in black, EWNP synthetics in blue and NSNP synthetics in magenta. The models use the same smoothing coefficient of 1×10^{-6}.

Figure S3. Comparison of GPS data and GPS-only model displacement vectors for Panel (a) the EWNP and Panel (b) the NSNP (b). Residuals between the GPS-only model and GPS data are shown in Panels (c) and (d). The corresponding distributed slip models are shown by colour contours on the fault planes projected to the surface.

Figure S4. Slip distributions for the finite fault models using the Lange layered earth model illustrating the effect of variable smoothing coefficients. Panel (a) 5×10^{-9} smoothing coefficient for the GPS models and 2.5×10^{-6} smoothing coefficient for seismic and joint models (with equally weighted GPS and seismic data). Panel (b) 1×10^{-9} smoothing coefficient for the GPS models and 5×10^{-7} smoothing coefficient for seismic and joint models (with equally weighted GPS and seismic data). The EWNP slip distribution is more sensitive to the smoothing coefficient than NSNP, especially for the GPS models, and needs to have at least the values of smoothing in Panel (a) to have a continuous slip distribution.

Figure S5. Slip distributions for the Collings finite fault models illustrating the effect of variable smoothing coefficients. Panel (a) 5×10^{-9} smoothing coefficient for the GPS models and 1×10^{-6} smoothing coefficient for seismic and joint models (with equally weighted GPS and seismic data). Panel (b) 1×10^{-9} smoothing coefficient for the GPS models and 5×10^{-7} smoothing coefficient for seismic and joint models (with equally weighted GPS and seismic data). The EWNP slip distribution is still very sensitive to smoothing coefficient for the GPS models, but the seismic slip distribution is less sensitive than the Lange models and can have less imposed smoothing.

Figure S6. Slip distributions for the Collings finite fault models illustrating the effect of variable rupture velocity. Slower rupture velocity places higher peak slip near the hypocentre and focuses the slip distribution.

Figure S7. Comparison of joint finite fault model and point source model displacement vectors for Panel (a) the EWNP and Panel (b) the NSNP. The GPS data variance reduction decreases from 79 per cent (EWNP) and 78 per cent (NSNP) to 68 per cent for the point source model.

Figure S8. Comparison of synthetics for the preferred joint finite fault model (EWNP) and a point source model. The data is plotted in black, EWNP synthetics in blue and point source synthetics in magenta. The total seismic variance reduction decreases from 66 to 10 per cent when switching from the finite fault to point source model.

Figure S9. Stress changes resolved on the EWNP fault geometry, resulting from Panel (a) the 2005 backthrust cluster (Wiseman *et al.* 2011), Panel (b) the 2007 M_w 7.9 Bengkulu aftershock (Konca *et al.* 2008), Panel (c) the 2009 backthrust cluster (Wiseman *et al.* 2011) and Panel (d) all the recent backthrust and megathrust events (including 2004, 2005 and 2007 megathrust earthquakes that

individually had ΔCFS < 5 kPa). The cross-sections are perpendicular to the trench and extend through the 2009 hypocentre (profile A–A′ shown on Fig. S10). Intraslab earthquake focal mechanisms following each potential triggering event, up to and including the 2009 Padang earthquake, overlay the cross-sections. Note the nonlinear stress scale.

Figure S10. Stress changes resulting from slip on the NSNP resolved on the megathrust. The map shows CFS change on the megathrust assuming $\mu' = 0.4$. The cross-sections are perpendicular to the trench and extend through the 2009 hypocentre and show shear stress change, normal stress change and CFS change.

Table S1. Continuous GPS station coordinates and observed displacements (mm) due to the 2009 September 30 Padang earthquake.

Table S2. Continuous GPS station coordinates and modelled displacements (mm) due to the 2009 September 30 Padang earthquake, using the preferred east–west nodal plane joint model.

Table S3. Continuous GPS station coordinates and modelled displacements (mm) due to the 2009 September 30 Padang earthquake, using the north–south nodal plane joint model.

Table S4. The Lange earth model. The velocity structure is from Lange *et al.* (2010), the densities from Pollitz *et al.* (2006) and attenuation quality factors are from PREM (Dziewonski & Anderson 1981).

Table S5. The Collings earth model with a V_p/V_s ratio of 1.85. The velocity structure is from Collings *et al.* (2012), the densities from Pollitz *et al.* (2006) and attenuation quality factors are from PREM (Dziewonski & Anderson 1981).

Please note: Wiley-Blackwell are not responsible for the content or functionality of any supporting materials supplied by the authors. Any queries (other than missing material) should be directed to the corresponding author for the article.